Available online at www.sciencedirect.com

ScienceDirect

J Materiomics 2 (2016) 280–289

www.ceramsoc.com/en/

www.journals.elsevier.com/journal-of-materiomics/

On the relevance between fine structure and enhanced performance of skutterudite thermoelectric materials: X-ray spectroscopy studies

Ping Wei, Wenyu Zhao*, Dingguo Tang, Wanting Zhu, Xiaolei Nie, Qingjie Zhang**

State Key Laboratory of Advanced Technology for Materials Synthesis and Processing, Wuhan University of Technology, Wuhan, 430070, China

Received 18 April 2016; revised 2 June 2016; accepted 3 June 2016
Available online 18 June 2016

Abstract

The relevance between the fine structure and transport performance of thermoelectric materials can be revealed by X-ray spectroscopy including X-ray absorption and emission spectra as an effective tool. In this paper, the experimental spectra of extended X-ray absorption fine structure (EXAFS), X-ray absorption near-edge structure (XANES), and valence-band X-ray photoelectron spectroscopy (XPS) of Ba and In double-filled skutterudites ($Ba_xIn_yCo_4Sb_{12}$) were analyzed *via* the first-principles calculation and spectrum simulation. The atomic-scale fine structures indicate that the rectangle Sb_4 rings become square when the total filing fraction of Ba and In increases. The transition of Sb_4 rings leads to the band convergence and density of states (DOS) increase of the Sb–Sb $pp\sigma$ bonding and $pp\pi^*$ antibonding states. The enhanced TE performance of $Ba_xIn_yCo_4Sb_{12}$ is essentially attributed to the band convergence, the increased DOS near the Fermi level, and the resonant phonon scattering of Ba and In fillers.

Keywords: Thermoelectric materials; X-ray absorption near-edge structure; Extended X-ray absorption fine structure; Band convergence

1. Introduction

Thermoelectric (TE) materials provide a fully solid-state solution for direct and reversible conversion from heat to electricity, showing a great potential in the applications of power generation and cooling [1,2]. The performance of a TE material is governed by the dimensionless figure of merit $ZT = S^2\sigma T/\kappa$, where σ is the electrical conductivity, S the Seebeck coefficient, T the absolute temperature, and κ the thermal conductivity, which comprises an electronic (κ_e) component and a lattice (κ_l) component. Exploring materials that possess both a high power factor ($S^2\sigma$) and a low thermal conductivity is a key to developing high-performance TE materials. However, the realization of high TE performance is challenging since these TE properties are strongly interdependent, which are fundamentally determined by the atomic-scale fine structure, electronic structure, and the scattering mechanisms of electrons and phonons [3,4]. In the past decades, various strategies have been developed to optimize TE performance. It has been demonstrated that the lattice thermal conductivity can be suppressed by several approaches such as alloying [5], nanostructure engineering [6], and intrinsically large anharmonic lattice [7–9]. As the κ_l values of some TE materials have been reduced towards their amorphous limits [7–10], there is an increasing interest in optimizing the electrical properties by engineering the band structure or changing the energy dependence of carrier transport [11–20]. For instance, improved power factor can be realized by creating localized resonant states near the Fermi level [11,12], increasing the band degeneracy *via* adjusting the temperature

* Corresponding author.
** Corresponding author.
E-mail addresses: wyzhao@whut.edu.cn (W. Zhao), zhangqj@whut.edu.cn (Q. Zhang).
Peer review under responsibility of The Chinese Ceramic Society.

http://dx.doi.org/10.1016/j.jmat.2016.06.001

or composition [15–17], or by changing the carrier scattering mechanisms *via* energy filtering effect or introducing additional scattering [18–20]. Therefore, for a specific TE material, an in-depth understanding of the atomic-scale fine structure and electronic structure is fundamentally important in optimizing the transport properties.

The good TE performance and thermal stability of skutterudite $CoSb_3$ make it suitable for the large-scale application in mid-temperature power generation [21–23]. Binary $CoSb_3$ crystallizes in an open cubic structure, which is characterized by $CoSb_6$ octahedra, Sb_4 rectangle rings, and large Sb-icosahedral voids, as shown in Fig. 1. The oversized icosahedral voids can be filled with foreign atoms *A* (*A* can be alkali metal, alkali earth metal, rare earth metal, and other species such as Tl and In) to form filled skutterudites $A_xCo_4Sb_{12}$. The foreign atoms (so-called fillers) in the voids are weakly bonded with the surrounding Sb, rendering $CoSb_3$ very low κ_l due to the strong resonant phonon scattering [3,22]. Meanwhile, incorporating different kinds and amounts of fillers to the lattice of $CoSb_3$ enables a wide tuning of carrier concentration. Based on the rigid band approximation, which assumes that the fillers should have no significant effect on the band structure, the carrier concentration, at which the optimized power factor is obtained, should be on the order of 10^{20} cm^{-3} [23]. This approximation is instructive to optimize the power factor of most $CoSb_3$. Nevertheless, in some specific cases, the electronic structure of filled $CoSb_3$ is sensitive against the carrier concentration and the fillers, leading to unusual transport behavior [17,24,25]. One of the specific cases has been demonstrated in In-filled $CoSb_3$ where the coexistence of multiple localized effects was proposed to be responsible for the good TE performance [26]. The multiple localized effects include: i) the increase in localized density of states (DOS), ii) the accelerated electron movement, and iii) the heat-carrying phonon resonant scattering. Also found is that an incorporation of Ba into the In-filled $CoSb_3$ led to better TE performance [27,28]. However, the influences of atomic-scale fine structure and electronic structure on the transport properties of Ba and In double-filled $CoSb_3$ are still not well understood. In this work, by means of X-ray photoelectron spectroscopy (XPS) and X-ray absorption fine structure (XAFS), and combining with theoretical calculation, we have carried out a thorough study on the atomic-scale fine structure and electronic structure of Ba and In double-filled skutterudites

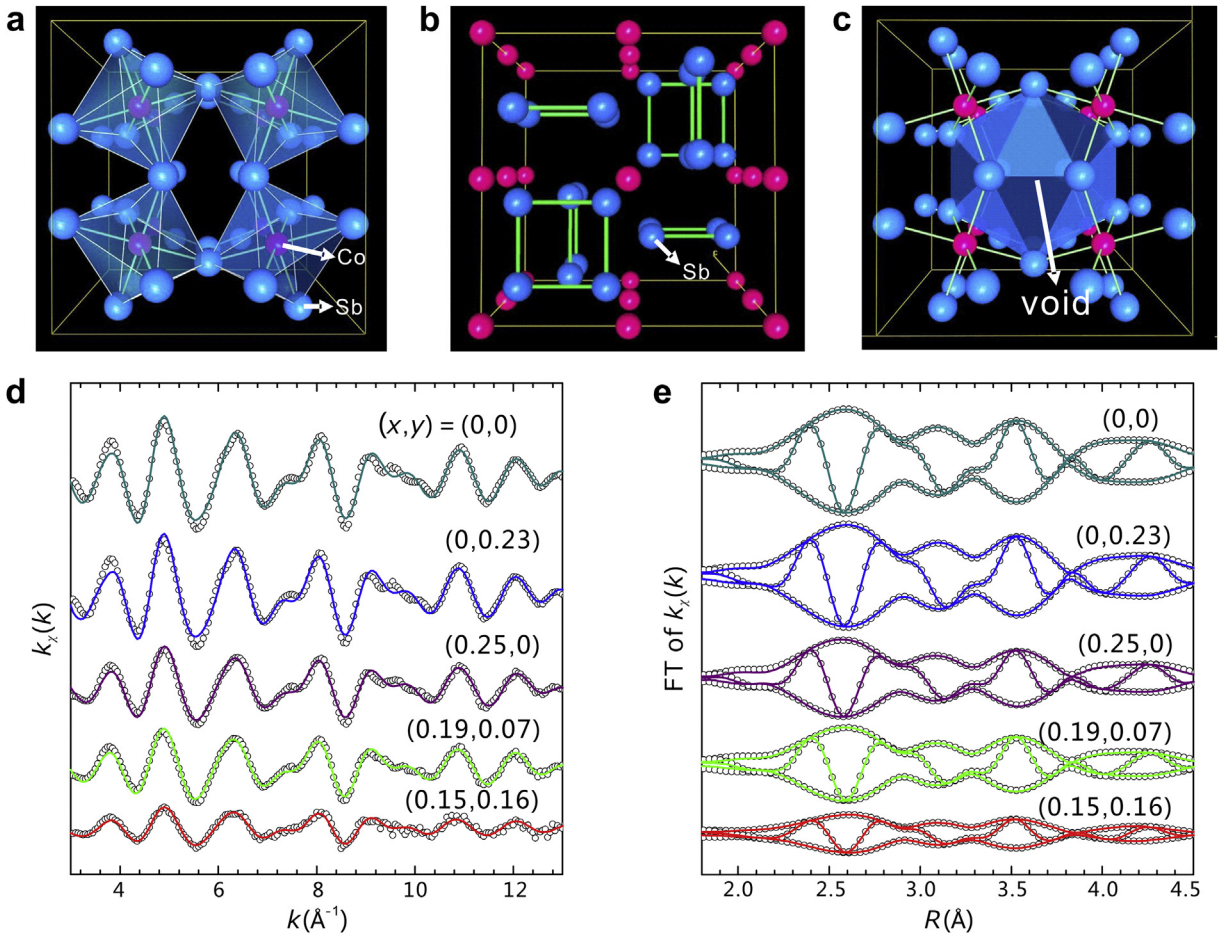

Fig. 1. **Crystal structure of $CoSb_3$ and EXAFS modeling of $Ba_xIn_yCo_4Sb_{12}$.** The crystal structure of $CoSb_3$ consists of (a) $CoSb_6$ octahedra, (b) Sb_4 rings, and (c) Sb-icosahedral voids which allow the accommodation of foreign atoms to form filled $CoSb_3$. Experimental (circles) and simulated (lines) (d) *k*-weighted Sb *K*-edge EXAFS spectra and (e) the Fourier transformed spectra for $Ba_xIn_yCo_4Sb_{12}$.

$Ba_xIn_yCo_4Sb_{12}$, with the aim of revealing the physical mechanisms underlying the improved TE performance. The theoretical and experimental results indicate that the DOS of the Sb–Sb $pp\sigma$ bonding and $pp\pi^*$ antibonding states of the Sb_4 rings were increased in Ba and In double-filled $CoSb_3$. This behavior is caused by the atomic-scale fine structure changes of the rectangle Sb_4 rings which trend to be squarer upon filling. These atomic-scale fine structure and electronic structure variations are responsible for the improved power factor as experimentally observed in Ba and In double-filled $CoSb_3$.

2. Experiments and calculations

2.1. Materials and methods

Single-phase unfilled $CoSb_3$ and filled skutterudites $Ba_xIn_yCo_4Sb_{12}$ ($0 \le x \le 0.3$, $0 \le y \le 0.3$) were synthesized by the combination of melt-quenching, annealing, and spark plasma sintering (SPS). The synthesis procedure, phase determination, and TE properties were reported in previous work [27,28]. The actual filling fractions (x and y) of $Ba_xIn_yCo_4Sb_{12}$ were determined by a model JXA-8100 electron probe microanalyzer (EPMA). The collection of valence-band spectra was performed on a model VG Thermo Multilab 2000 X-ray photoelectron spectrometer (XPS), using a monochromatic Al K_α line with a photon energy of 1486.6 eV and a 180° hemispherical analyzer in a constant-resolution mode with a pass energy of 25 eV. The energy resolution was determined to be 0.6 eV based on the analysis of the Ag Fermi edge. The energy step size and spot size were kept at 0.05 eV and OFF. Before spectrum collection, the samples with polished surface were loaded into an ultrahigh vacuum analyzer chamber (10^{-6}–10^{-7} Pa) and then bombarded with Ar-ion beam until no trace of contamination.

The XAFS measurements involved X-ray absorption near-edge structure (XANES) and extended X-ray absorption fine structure (EXAFS), which were performed in a model BL14W1 beamline in Shanghai synchrotron radiation facility (SSRF). The storage ring was working at 3.5 GeV and 300 mA. Si (111) double-crystal monochromater with an energy resolution of 1.5×10^{-4} eV at 10 keV was used for Co K-edge and Ba L_{III}-edge XAFS measurements. Si (311) double-crystal monochromater with an energy resolution of 0.5×10^{-4} eV at 10 keV was used for Sb K-edge and In K-edge measurements. Before measurements, the powder samples were passed through a 400 mush sieve and then brushed onto a thin Kapton tape for Co K-edge and Ba L_{III}-edge measurements. In the case of Sb K-edge and In K-edge measurements, the sieved powder mixed with LiF powder was pressed to pellets with uniform thickness. All the XAFS spectra were collected in the transmission mode at room temperature. The energy calibration was monitored using metal Co, Sb, and In foils for their K-edge measurements and metal Ti foil for Ba L_{III}-edge. The data treatments including background subtraction, normalization, and derivative were carried out on the IFEFFIT program [29].

2.2. Theoretical calculations

The first-principles calculations of ground-state electronic structure of $CoSb_3$ were performed using density-functional theory (DFT) with norm-conserving pseudo-potentials, as implemented in the CASTEP package [30]. Lattice relaxation and structural optimization were first carried out through total energy calculations. Spin-orbit effect was not taken into account [31,32]. A $2 \times 1 \times 1$ supercell was used and the Monkhorse-Pack grid for the Brillouin zone was set as $4 \times 4 \times 4$. To extract atomic-scale fine structures from experimental spectra of Sb K-edge EXAFS, the theoretical spectra were calculated with the IFEFFIT package [29] based on the reported $CoSb_3$ structure [33]. The scattering path, scattering spherical potential, and phase shift were determined by the FEFF9 code [34]. The scattering amplitudes contributed from the fillers were neglected for the low concentration and low scattering intensity of Ba and In (<5%). The scattering amplitudes and thermal vibration parameters for the Sb–Sb long pair and short pair in the Sb_4 ring were assumed to be identical due to their same atomic coordination and close distances [35].

3. Results and discussion

3.1. Atomic-scale structure of filled $CoSb_3$

Skutterudite $CoSb_3$ crystallizes in a body-centered cubic structure with space group Im-3. Each unit cell contains eight $CoSb_6$ octahedra cornered by Sb atoms as shown in Fig. 1a, and the twelve nearest Sb atoms form icosahedral voids which distribute the body center and eight corners of unit cell as shown in Fig. 1c. In many cases, the crystal structure of $CoSb_3$ is shown as Fig. 1b, where each unit cell is made of eight sub-cubes cornered by Co atoms, and six of which are occupied by planar Sb_4 rectangle rings, leaving the other two empty. The centers of the empty sub-cubes are the sites where the fillers reside, which in fact are the centers of the icosahedral voids surrounded by the twelve nearest Sb atoms. For filled skutterudites, the structural parameters such as the sizes of the icosahedral voids and the rectangle rings are important in studying the structural response to filling.

EXAFS has been used to determine the atomic-scale fine structure of caged TE materials such as skutterudites and clathrates [35,36]. Here, it was used to discern the geometrical changes of the Sb_4 rings in $CoSb_3$ as a response to the filling. The k-weighted spectra and the Fourier transforms over a k range from 3 to 13 $Å^{-1}$ of the measured EXAFS spectra are shown in Fig. 1d and e. It can be seen that the filling with Ba and In has noticeable effect on the total scattering amplitudes, which gradually decrease with more filling. These experimental results can be explained with the large thermal vibration parameters of filling atoms and the enlarged lattice parameters [28]. Table 1 shows the distances of the nearest Co–Sb pairs (R) and Sb–Sb short (R_1) and long pairs (R_2) obtained from simulations. Filling Ba and In has less impact on the distance of Co–Sb pairs although it can remarkably change the distance of Sb–Sb short and long

Table 1
Structure parameters of $Ba_xIn_yCo_4Sb_{12}$ based on EXAFS modeling. The error for distances is ±0.02 Å.

Samples	R(Co–Sb) (Å)	R_1 (Å)	R_2 (Å)	R_2-R_1 (Å)	R_2:R_1
$CoSb_3$	2.52	2.87	3.03	0.16	1.06
$In_{0.23}Co_4Sb_{12}$	2.52	2.88	3.03	0.15	1.05
$Ba_{0.25}Co_4Sb_{12}$	2.52	2.84	2.92	0.08	1.03
$Ba_{0.19}In_{0.07}Co_4Sb_{12}$	2.53	2.88	2.92	0.04	1.01
$Ba_{0.15}In_{0.16}Co_4Sb_{12}$	2.53	2.90	2.93	0.03	1.01

pairs. For unfilled $CoSb_3$, a large distance difference of R_1 and R_2 (R_2-R_1) was detected, which is in reasonable agreement with the intrinsic rectangle Sb_4 rings [37]. For In-filled $In_{0.23}Co_4Sb_{12}$, R_1 and R_2 show small changes as compared to these of $CoSb_3$, and the similar trend was reported based on X-ray single crystal data of In-filled $CoSb_3$ [38], despite a discrepancy of distances R_1 and R_2 can be found in these two individual analysis. The discrepancy could be attributed mainly to the samples which were synthesized by different methods. In the case of Ba-filled $Ba_{0.25}Co_4Sb_{12}$, R_2 shrinks significantly. As a consequence, the distance difference of R_1 and R_2 and the square ratio of the Sb_4 rings (R_2:R_1) reduce considerably, confirming the squarer Sb_4 rings in Ba-filled $Ba_{0.25}Co_4Sb_{12}$ [27]. When filling with Ba and In, R_2 is enlarged slowly, while R_1 is increased remarkably and gets close to R_2 gradually. As a result, their difference in $Ba_{0.15}In_{0.16}Co_4Sb_{12}$ is almost zero within the errors, and accordingly the square ratio is reduced significantly from 1.06 for $CoSb_3$ to 1.01 for $Ba_{0.15}In_{0.16}Co_4Sb_{12}$. These results clearly signify the structural transition of the Sb_4 rings from rectangle to square as a response to the double-atom filling. The square rings were also reported in Tl-filled and Ce-filled skutterudites from the structural refinements based on experimental diffraction data [37,39]. The theoretical work indicated that the size of Sb_4 rings might have an influence on the band structure of filled skutterudites, especially near the Fermi level [32]. However, a fundamental understanding on the effect of the local structural transition on the electronic structure is still inadequate. Therefore, the following section deals with the electronic structure evolution in Ba and In double-filled $CoSb_3$.

3.2. Valence-band electronic structure of $Ba_xIn_yCo_4Sb_{12}$

The electronic structure of $CoSb_3$ is closely related to the bonding feature [40,41], where twelve 5*p* states in the rectangle Sb_4 rings form *ppσ* long and *ppσ* short bonds in the plane of rings and *ppπ* bonds perpendicular to the plane. The perpendicular Sb 5*p* states also involve in the formation of $CoSb_6$ octahedron with nearby Co in the form of d^2sp^3 hybridization. The valence band top and the conduction band bottom are mainly derived from the Co 3*d* and Sb 5*p* electrons [42,43]. Fig. 2a shows the ground-state partial density of state (PDOS) of $CoSb_3$. The valence-band structure of $CoSb_3$ can be described as a combination of eight component

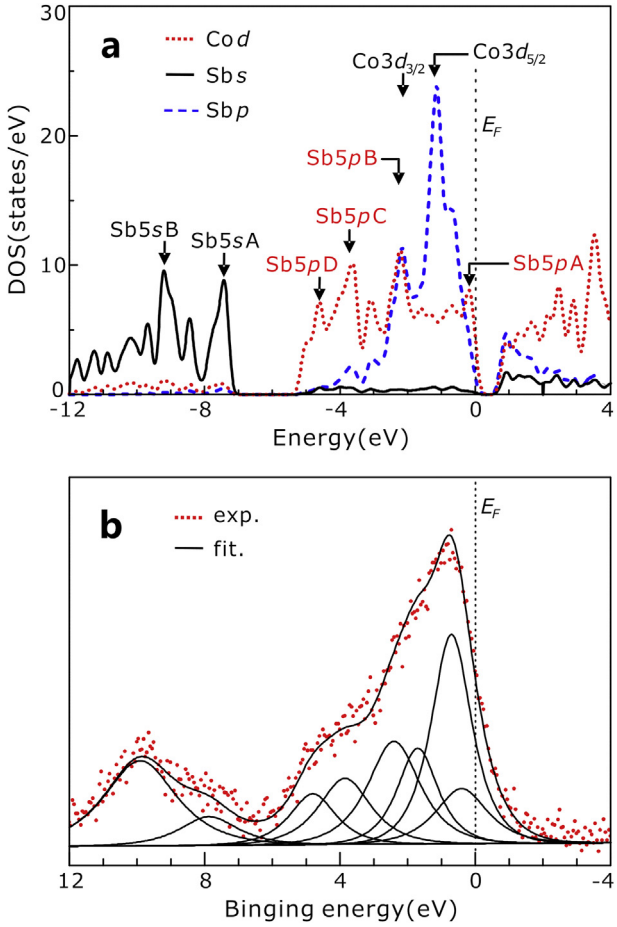

Fig. 2. **Valence-band electronic structure of $CoSb_3$.** (a) PDOS of unfilled $CoSb_3$ calculated with first-principles theory. Eight component states used to describe the valence band structure of $CoSb_3$ are labeled. (b) Experimental valence-band XPS spectrum of $CoSb_3$ (dots) was fitted with the eight component states using the combined Gaussian and Lorentzian profiles (solid lines).

states. The valence band bottom is composed of Sb 5*s* A (−9 to −6 eV) and Sb 5*s* B (−12 to −9 eV) states. The middle of valence band consists of two component states Sb 5*p* C (−4 to −2.5 eV) and Sb 5*p* D (−6 to −4 eV), which are arisen from the hybridized *ppσ* bonding states in Sb_4 rings. The top of valence band, with main contributions from the states of Co 3*d* and Sb 5*p* electrons, is attributed to the d^2sp^3 hybridization of $CoSb_6$ octahedron. Four different component states at the top of valence band can be distinguished and denoted as Sb 5*p* A (−1 to 0 eV), Co $3d_{5/2}$ (−1.5 to −0.5 eV), Co $3d_{3/2}$ (−2.5 to −1.5 eV), and Sb 5*p* B (−2.5 to −1.5 eV). The states Co $3d_{3/2}$ and Co $3d_{5/2}$ are localized, showing an intense spin-orbit splitting induced by the $CoSb_6$ octahedral crystal field, which is in agreement with the previous reports [44,45]. The contributions of Co 4*s* and Co 4*p* states to valence-band DOS can be neglected due to the low magnitude and broad dispersion. It is pointed out that the states near the Fermi level can be contributed to the Co 3*d* and Sb 5*p* electrons, which are in agreement with the calculated data [40,41].

Fig. 2b shows the experimental valence-band spectrum of $CoSb_3$ after subtracting a smooth Shirley-type background. The spectrum was deconvoluted with the eight component states according to the theoretical valence-band structure as proposed above. For each component state, the peak profile was mixed with the Gaussian and Lorentzian functions with an area ratio of 20:80, which was used to account for the spectrometer resolution and the lifetime broadening of photoelectrons, respectively [27]. At different lifetime broadenings, the full width at half maximum is 1.4 eV, 1.6 eV, and 2.0 eV for Co3*d*, Sb 5*p*, and Sb 5*s* electrons, respectively. All the spectral features were well reproduced with the combination of eight component states. It can be found that the energies of the eight component states are in reasonable agreement with the calculated values, as shown in Fig. 2a. Note that the Co $3d_{5/2}$ and Co $3d_{3/2}$ show energies of 0.7 and 1.7 eV, separated by a spin-orbit splitting of 1.0 eV, which is consistent with the calculated value. The number of valence electron (C_i) for each component state can be determined by the integral intensity of the experimental valence-band spectra,

$$C_i = T_e \cdot [I_i/(\sigma_i \lambda_i)] \Big/ \left[\sum_{j=1}^{n} I_j/(\sigma_i \lambda_i) \right] \quad (1)$$

where T_e is the total valence electrons of the measured compound, n is the number of component states in the valence band, λ_i the inelastic electron mean free path for a constituent atom i, σ_i the photoionization cross-section of atom i. The total valence electron number in $CoSb_3$ is 96 per each unit cell. λ_i is 24.0 Å and 30.4 Å for Co and Sb. Since the incident photon energy is 1486.6 eV, σ_i has a value of 0.16 and 0.11 for Co $3d_{5/2}$ and $3d_{3/2}$ electrons, and 0.08 and 0.11 for Sb 5*p* and 5*s* electrons, respectively [42]. For $CoSb_3$, 62.5% of the valence electrons occupy the top region of the valence-band, while the valence electrons in the middle and bottom regions are almost equal (i.e., 18.6% and 18.8%), indicating that the largest contribution to the valence-band originates from the $CoSb_6$ octahedron. The Co $3d_{5/2}$ contains over 26% of the total valence electrons, reflecting a strong localized nature of Co 3*d* electrons.

The electronic structure of filled skutterudites $Ba_xIn_yCo_4Sb_{12}$ was examined by valence-band XPS spectra. Fig. 3 shows the measured valence-band spectra of $Ba_xIn_yCo_4Sb_{12}$. In order to achieve clear evidence on the valence band changes, the experimental spectra were numerically modeled using the same configuration of eight component states. The rationality of this modeling used for Ba-filled is understandable since Ba has no valence electron in the valence band and instead donates two electrons to the framework. For In-contained $CoSb_3$, the rationality is since i) the atomic percentage of In fillers is much smaller than those of Co and Sb; ii) for two In 5*s* electrons contributing to the valence band, one has localized feature and another is delocalized [26]; and iii) the photoionization cross-section of In (0.02) is much smaller than those of Co and Sb (about 0.1) [42]. Therefore, the measured valence-band XPS spectra can clearly detect the electronic states contributed from Co and Sb framework

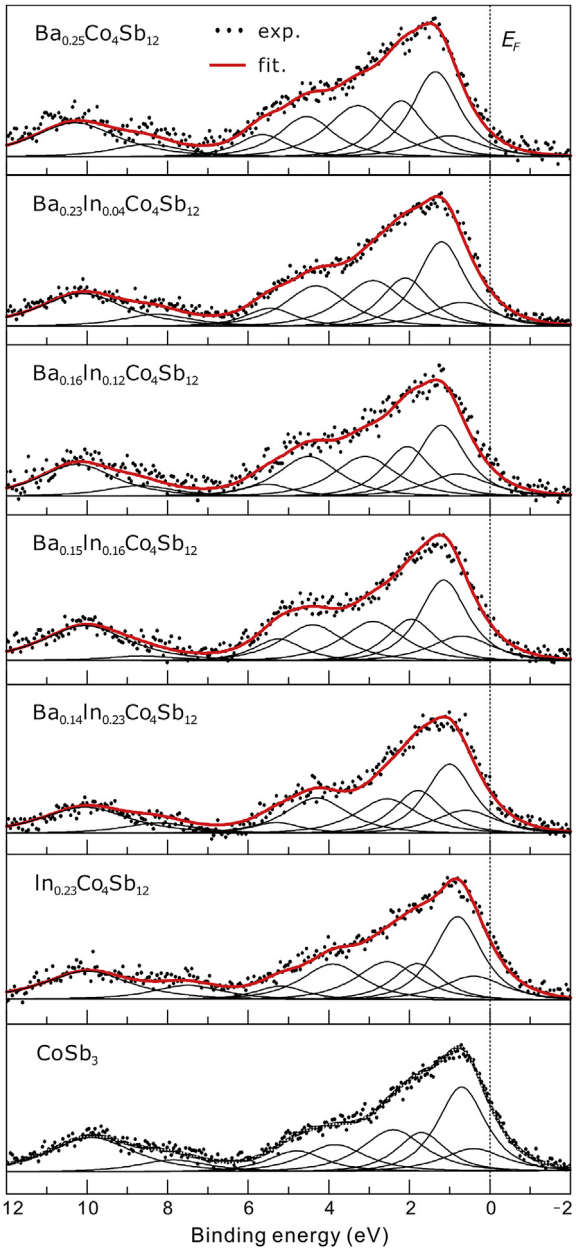

Fig. 3. **Valence-band spectra of $Ba_xIn_yCo_4Sb_{12}$.** The experimental data (dots) are fitted with eight component states using the combined Gaussian and Lorentzian profiles (solid lines).

atoms. Fig. 3 also shows the modeling of the valence-band XPS spectra of $Ba_xIn_yCo_4Sb_{12}$. For $Ba_xIn_yCo_4Sb_{12}$, the valence electron number is $96 + 2x + y$ when considering the chemical state of Ba and In is divalent and monovalent, respectively [28]. The energy position (P) and valence electron number (C_i) for each component state for $Ba_xIn_yCo_4Sb_{12}$ compounds can be hence determined.

Ba and In fillings cause a chemical shift (δ) in the valence-band XPS spectra. The peak position of Co $3d_{5/2}$ component state shifts towards high binding energy side by $\delta = 0.1$ eV for In-filled $In_{0.23}Co_4Sb_{12}$, and to higher binding energy when Ba filling fraction (x) increases and In filling fraction (y) decreases. The largest shift is $\delta = 0.65$ eV for Ba-filled

$Ba_{0.25}Co_4Sb_{12}$. Other component states show the similar tendency. The different energy shifts for Ba- and In-contained filled $CoSb_3$ reflect their different donor abilities since Ba filler is purely ionic and denotes two electrons to the conduction band, while In filler is covalently bonded with surrounded Sb atoms with a monovalent configuration. The chemical shift is also supported by the carrier concentration variations [27]. The effect of In filler on the electronic structure of $CoSb_3$ is more complicated than the effect of alkali and alkali earth metals [26,27].

To clarify the effect of the filling fraction of Ba and In (x and y) on the valence-band structure of $Ba_xIn_yCo_4Sb_{12}$, the component states, which belong to the same chemical bonds, are merged together. For instance, the component states Co $3d_{5/2}$ and Co $3d_{3/2}$ originating from the $CoSb_6$ octahedron are merged into Co 3*d*. The Sb 5*p* A and Sb 5*p* B corresponding to the Co–Sb bonds of $CoSb_6$ octahedron are designated as Sb 5*p* A + B. The Sb 5*p* C and Sb 5*p* D involving in the Sb–Sb bonds of Sb_4 ring are merged into Sb 5*p* C + D. The Sb 5*s* A and Sb 5*s* B become into Sb 5*s* A + B. After this treatment, the valence-band structure of $Ba_xIn_yCo_4Sb_{12}$ now is composed of four combined states, which are Co 3*d*, Sb 5*p* A + B, Sb 5*p* C + D, and Sb 5*s* A + B. Fig. 4 shows the valence electron number for each combined state as a function of filling fraction (x and y). For unfilled $CoSb_3$, the valence electron numbers of Co 3*d* and Sb 5*s* A + B are 32.2 and 17.9, which are in agreement with the theoretical values of 32.4 and 19.2, respectively. The Sb 5*p* A + B and Sb 5*p* C + D states possess valence electron numbers of 27.2 and 18.7, the sum of them is very close to the theoretical value of 44.4. These results validate the merging treatment.

Compared to unfilled $CoSb_3$, In-filled $In_{0.23}Co_4Sb_{12}$ exhibits small changes in the valence electron numbers, showing a slight increase in the Sb 5*p* C + D states and correspondingly a small decrease in the Sb 5*s* A + B states. The valence electron number of Sb 5*p* C + D firstly increases and then decreases slowly with increasing the filling fraction of Ba and decreasing that of In. The maximum for $Ba_{0.15}In_{0.16}Co_4Sb_{12}$ can be obtained, which is greater than that of the unfilled $CoSb_3$. The valence electron numbers of Co 3*d* and Sb 5*p* A + B states are almost unchanged upon filling. The reason is attributed to the weak interaction between the fillers and Co because of the strong charge screening effect of the large Sb-icosahedrons. The valence electron number of the Sb 5*s* A + B states slowly decreases and then keeps unchanged. It is assumed that a part of the Sb 5*s* nonbonding states should transfer into the bonding states as induced by the structural change of Sb_4 rings.

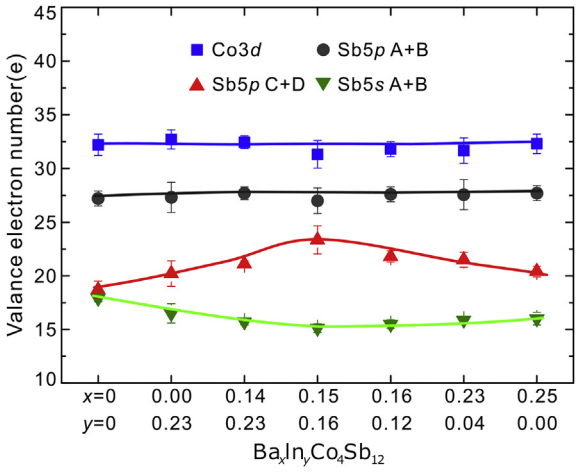

Fig. 4. Valence electron number changes of the four component states of $Ba_xIn_yCo_4Sb_{12}$ at different filling fractions.

As is shown above, the filling has an influence on the valence band of $CoSb_3$ in terms of increasing the valence electron number of Sb 5*p* C + D states, which involve in the *ppσ* bonds of the Sb_4 rings, but no effect on the electronic states of the $CoSb_6$ octahedra. The EXAFS analysis indicates that the Sb_4 rings of $CoSb_3$ gradually change the shape from rectangle to square and the structure of $CoSb_6$ octahedra keeps fixed when the total filling fraction increases. Note that the square ratio of Sb_4 ring is reduced from 1.06 for $CoSb_3$ to 1.01 for $Ba_{0.15}In_{0.16}Co_4Sb_{12}$, indicating an improved symmetry. As a consequence, the short and long *ppσ* bonds of the rectangle Sb_4 rings, with a relatively large bond length difference (i.e., 2.87 Å and 3.03 Å) in $CoSb_3$, gradually become identical as the total filling fraction increases. Accordingly, the two separate groups of electronic bands deep in the valence band of $CoSb_3$, contributed by the bonding states of the short and long *ppσ* bonds, gradually converge in energy due to the improved symmetry of the Sb rings. The occurrence of band convergence deep in the valence band can reasonably explain the increase in the valence-band DOS. For $Ba_{0.15}In_{0.16}Co_4Sb_{12}$ in which the Sb_4 rings are square, a significant convergence and a great increment of valence electron number of Sb 5*p* C + D states thus can be expected. Therefore, the increased electron number of the Sb 5*p* C + D states is attributed to the band convergence of the *ppσ* electronic states.

3.3. Conduction-band electronic structure of $Ba_xIn_yCo_4Sb_{12}$

XANES technique is a powerful tool in detecting the low-energy excited photoelectrons when undergoing the transition from the core-level states to the unoccupied states. The absorption feature of XANES spectrum mainly depends on the unoccupied states in the conduction band and a weak perturbation from core-hole interaction due to the highly localized character of the core-level electrons. In the case of $CoSb_3$, the core-hole interaction is fully suppressed by screening effect due to a great amount of valence electrons [46]. The conduction-band electronic structure of $CoSb_3$ can be thus detected by XANES technique. The theoretical results shown in Fig. 2 indicate that the lowest unoccupied states near the Fermi level are composed of Co 3*d* and Sb 5*p* states, which is assigned to the mixture of Co e_g^* and Co 3*d*–Sb 5*p* antibonding states, as resulted from the d^2sp^3 hybridization in the $CoSb_6$ octahedra and the *ppπ** antibonding states in the Sb_4 rings [44]. Fig. 5 shows the experimental spectra of Co and Sb *K*-edge XANES of

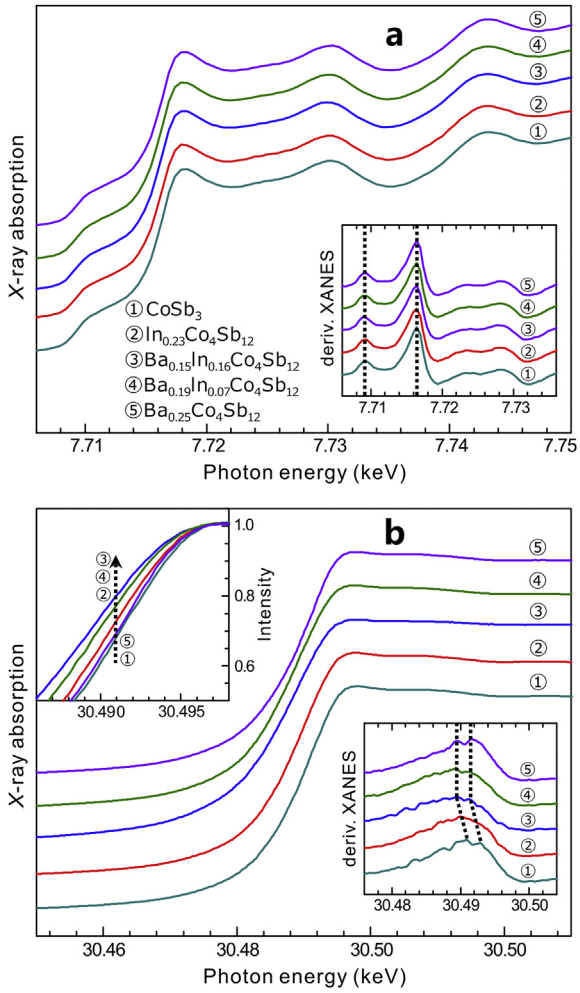

Fig. 5. **Co *K*-edge and Sb *K*-edge XANES spectra**. Experimental spectra of (a) Co *K*-edge and (b) Sb *K*-edge XANES of $Ba_xIn_yCo_4Sb_{12}$. The first derivative curves are plotted in the right insets in which the first and second inflection points are denoted with dashed lines. The left inset of the plot (b) shows the comparison of Sb *K*-edge XANES spectra with an energy shift towards high energy side by δ ($0 \leq \delta \leq 0.65$ eV). The δ value for each compound is determined by XPS valence-band spectra.

$Ba_xIn_yCo_4Sb_{12}$. The first inflection points of these spectra are shown in the right insets of Fig. 5. The first inflection points of Co and Sb *K*-edge spectra locate at 7709 and 30,491 eV, respectively, which are identical with those of the elemental Sb and Co [47]. For XANES, the first inflection point represents the transition starting from the core-level electron to the lowest unoccupied states. According to the dipole transition rule, the *K*-edge absorption is arisen from the $1s \rightarrow np$ transitions. In the case of Co *K*-edge XANES, the first inflection point of the pre-edge peak is caused by the dipole forbidden $1s \rightarrow 3d$ transitions with a small contribution from the Co $3d-4p$ hybridization, which is linked to the inversion symmetry breaking in the distorted $CoSb_6$ octahedron. Therefore, the metallic-like feature of the inflection point of the Co *K*-edge XANES proves that the unoccupied Co $3d$ states essentially situate near the Fermi level, which is consistent with the calculated value [46]. The main absorption peak near 10 eV greater than the pre-edge peak is originated from the unoccupied Co $4p$ states with the dipole $1s \rightarrow 4p$ transitions. The absorption spectra of unfilled and filled $CoSb_3$ are similar. The first inflection points and absorption intensity of Co *K*-edge XANES spectra are almost identical, indicating the small effect of Ba and In filling on the unoccupied Co $3d$ states. This phenomenon is due to the stiff framework of $CoSb_6$ octahedron as determined by the former EXAFS analysis, which further confirms the slight influence of filling on the electronic structure of the $CoSb_6$ octahedron.

For the Sb *K*-edge XANES spectra, the absorption edge and main peak both can be attributed to $1s \rightarrow 5p$ transitions, while the absorption peaks at the greater energy side correspond to the transitions from the Sb $1s$ core-level states to the unoccupied Co $4p$ states due to the existence of d^2sp^3 orbital hybridization in $CoSb_6$ octahedron. The derivative curves exhibit double inflection points near the absorption edge. The first inflection point refers to the position of the lowest unoccupied Sb $5p$ states, which are close to the Fermi level. The second inflection point, which is about 2 eV greater than the first one, corresponds to the energy maximum of the unoccupied Sb $5p$ sates. It can be found that the first inflection point shifts toward a lower energy by 1.0 eV for In-filled $In_{0.23}Co_4Sb_{12}$, and by 2.0 eV for Ba and In double-filled $Ba_xIn_yCo_4Sb_{12}$. The energy shift towards a lower energy, which is attributed to the increased carrier concentration as observed in the Hall measurements [26,27].

The variations of absorption edge intensity can be an indicator of the number of unoccupied states [48,49], especially for the material systems in which the core-hole interaction can be fully suppressed, i.e., $CoSb_3$. The comparison of absorption edge intensity of the Sb *K*-edge XANES spectra of $Ba_xIn_yCo_4Sb_{12}$ is shown in the left inset of Fig. 5b. Since Ba and In are dopants and the Fermi level shifts from the band gap to the conduction-band bottom, the whole absorption spectra of $Ba_xIn_yCo_4Sb_{12}$ are intentionally shifted towards a higher energy side by an energy of δ ($0 \leq \delta \leq 0.65$ eV) to eliminate the effect of charge transfer. The δ values were determined from the above valence-band measurements, by calculating the energy shift of the Co $3d_{5/2}$ component state. This treatment is reasonable since the fillers bring out only a slight change in the band gap [32]. It can be seen that the absorption edge intensity of the Sb *K*-edge XANES spectra increases slightly for In-filled $CoSb_3$ and is considerably increased for Ba and In double-filled $CoSb_3$, indicating that the DOS of the unoccupied Sb $5p$ states is accumulated in $Ba_xIn_yCo_4Sb_{12}$. According to the former results, the unoccupied Sb $5p$ states in $CoSb_3$ are composed of two components, i.e., Co–Sb antibonding states in the $CoSb_6$ octahedron and Sb–Sb $pp\pi^*$ antibonding states in the Sb_4 ring. Since the electronic structure of $CoSb_6$ octahedron has no change with varying the filling fraction, any change in the unoccupied Sb $5p$ states must come from the variation of Sb–Sb $pp\pi^*$ antibonding states in the Sb_4 ring. Therefore, the DOS increase of the unoccupied Sb $5p$ states is attributed to the increased Sb–Sb $pp\pi^*$ antibonding states. Based on the former valence-band spectra analysis, we find that with increasing the filling fraction of Ba and In, the DOS

of Sb–Sb $pp\sigma$ bonding deep in the valence band and Sb–Sb $pp\pi^*$ antibonding states at the bottom of conduction-band both are improved, and the reasons of which both point to the band convergence caused by the improved symmetry of the Sb_4 ring.

Fig. 6 shows the In *K*-edge XANES spectra of $Ba_xIn_yCo_4Sb_{12}$ and metallic In foil. The inset shows the Ba L_{III}-edge XANES spectra of $Ba_{0.3}Co_4Sb_{12}$ and BaO. For $Ba_{0.3}Co_4Sb_{12}$ and BaO, the absorption white lines and the energy of main absorption peaks are similar. The inflection points of the white lines of Ba L_{III}-edge for $Ba_{0.3}Co_4Sb_{12}$ and BaO both locate at 5249 eV, which are greater than those of the standard metal Ba (5427 eV) by 2 eV [47], indicating the divalent Ba^{2+} in $Ba_{0.3}Co_4Sb_{12}$. For $In_{0.23}Co_4Sb_{12}$, the main absorption peak has the energy as that of In foil (i.e., 27,945.5 eV). This corresponds to the dipole $1s \rightarrow 5p$ transitions, indicating the covalent interaction of In with the host framework. The first inflection point of $In_{0.23}Co_4Sb_{12}$ is similar to that of the In metal at 27,940 eV (marked by dotted line), indicating that the unoccupied In 5*p* states locate close to the Fermi level, which is in agreement with the above calculations. For Ba and In double-filled $CoSb_3$, the first inflection points keep unchanged as the filling fraction of In increases, showing the Fermi pinning behavior of In 5*p* states. The Fermi pinning of In electrons was also found in In-doped PbTe system [50,51], which is supposed to be caused by the relatively localized feature of the unoccupied states of In electrons. Incorporating In into $CoSb_3$ leading to multiple localized effects has been recently clarified [26].

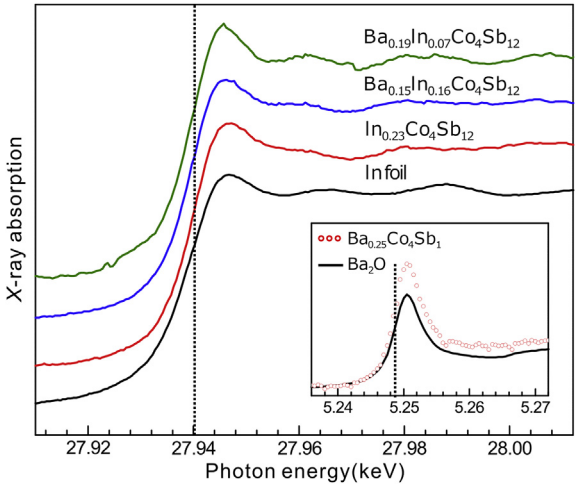

Fig. 6. **In *K*-edge and Ba L_{III}-edge XANES spectra**. Experimental spectra of In *K*-edge XANES are obtained from $Ba_xIn_yCo_4Sb_{12}$ and metallic In foil. The inset shows experimental spectra of Ba L_{III}-edge XANES for $Ba_{0.3}Co_4Sb_{12}$ and BaO. The first inflection points are denoted by dashed lines.

3.4. Enhanced thermoelectric properties in $Ba_xIn_yCo_4Sb_{12}$

For *n*-type materials, the electronic states situated at the conduction band bottom are responsible for the carrier transport properties especially for the electrical conductivity and the Seebeck coefficient. According to the Mott relation [52],

$$S = \frac{\pi^2 k_B}{3q} k_B T \left\{ \frac{d[\ln(\sigma(E))]}{dE} \right\}_{E=E_F} = \frac{\pi^2 k_B}{3q} k_B T \left\{ \frac{1}{n}\frac{dn(E)}{dE} + \frac{1}{\mu}\frac{d\mu(E)}{dE} \right\}_{E=E_F} \quad (2)$$

where n is the carrier concentration, μ the carrier mobility, q the charge of an electron, k_B the Boltzmann constant, and E_F the Fermi energy to describe the electron energy E at E_F. It can be seen that a rapid change in carrier concentration and/or mobility in a small energy interval close to the Fermi level is favorable for the enhanced Seebeck coefficient. Since $n(E) = f(E)g(E)$, where $f(E)$ is the Fermi integral determined by E_F and $g(E)$ is the DOS near the Fermi level, a strong energy dependence of DOS near the Fermi level is crucial for the Seebeck coefficient enhancement [53].

The results indicate that the filling of Ba and In can affect the DOS of conduction-band bottom in two aspects: i) the introduction of unoccupied In 5*p* localized states near the Fermi level and ii) the increased DOS of Sb–Sb $pp\pi^*$ antibonding states. The introduction of unoccupied In 5*p* states favors the optimization of the electrical transport properties due to its resonant-like behavior [26]. That is also the reason why In-filled $In_{0.23}Co_4Sb_{12}$ exhibits a higher power factor (i.e., ~38 μW K^{-2} cm^{-1}) at room temperature [28]. The occurrence of increased Sb–Sb $pp\pi^*$ antibonding states can be expected due to the increased Seebeck coefficient and maintained high electrical conductivity, thus which is favorable for power factor. The electrical transport properties measurements show that at 850 K $Ba_{0.15}In_{0.16}Co_4Sb_{12}$ and $Ba_{0.14}In_{0.23}Co_4Sb_{12}$ exhibit the maximum power factor (i.e., ~40 μW K^{-2} cm^{-1}) [27]. These experimental results further substantiate the benefits of the modified electronic states in improving the electrical properties.

The thermal conductivity measurements show that the decrease of lattice thermal conductivity is due to the rattling of fillers, which decreases from the unfilled $CoSb_3$ (~10 W m^{-1} K^{-1}), the Ba-filled $Ba_{0.25}Co_4Sb_{12}$ (4.7 W m^{-1} K^{-1}) and the In-filled $In_{0.23}Co_4Sb_{12}$ (3.1 W m^{-1} K^{-1}) to the Ba and In double-filled $Ba_{0.15}In_{0.16}Co_4Sb_{12}$(~1.5 W m^{-1} K^{-1}) at room temperature. These experimental results show that the weakly bounded fillers in the Sb-icosahedrons can effectively suppress the propagation of the heat-carrying phonons by creating intense resonant phonon scattering. In addition, the filling of Ba and In is more effective in reducing lattice thermal conductivity, as compared to the single-filled cases, which can be attributed to the wider range of phonon scattering frequency aroused by two distinct fillers [22]. Based on the electronic structure study, the physical mechanisms behind the enhanced TE performance in Ba and In double-filled $CoSb_3$ become clear, which are associated with three beneficial effects as following: i) the increased conduction-band DOS due to the band

convergence effect of the Sb–Sb $pp\pi^*$ antibonding states, ii) the localized feature of the unoccupied states of In 5*p* electrons near the Fermi level, and iii) the wide-frequency resonant phonon scattering created by distinct Ba and In fillers.

4. Conclusions

The EXAFS, XANES, and XPS techniques were employed to discern the underlying physical connections between the atomic-scale fine structure and electronic structure and the enhanced TE properties in Ba and In double-filled $CoSb_3$. The local structure evolution of Sb atoms from the EXAFS data indicated that the atomic-scale structural change of the Sb_4 rings occurred from rectangle to square as the total filing fractions increased. A combined solution for eight component states was proposed, which enabled a reasonable description of the valence-band electronic structure of $Ba_xIn_yCo_4Sb_{12}$. It was revealed that the filling of Ba and In had no effect on the electronic structure of $CoSb_6$ octahedron, but improved the DOS of the Sb–Sb $pp\sigma$ bonding and $pp\pi^*$ antibonding states of Sb_4 ring. The occurrence of electronic state degeneracy caused by the structural transition of the Sb_4 rings led to the increased DOS both at valance band and conduction band. Ba, as an ionic filler, donates all its valence electrons to the neighboring Sb, having less influence on the electronic structure. However, the filler In, which is covalently bonded with nearby Sb, brings about the modification to the electronic structure in a manifestation of creating localized electronic states and pinning the Fermi level. The improved TE properties of Ba and In double-filled $CoSb_3$ can be explained in terms of the three beneficial effects, including localized DOS increase, band convergence, and wide-frequency resonant phonon scattering as well.

Acknowledgments

This work was supported by the National Basic Research Program of China (973-program) (No. 2013CB632505), National Natural Science Foundation of China (Nos. 11274248, 51521001, 51572210, and 51502228). Special thanks are due to the beam line scientist at Shanghai synchrotron radiation facility (SSRF). The authors also want to thank Prof. Y. Gao from Hubei University and Prof. G. S. Shao from University of Bolton for the valuable discussion.

References

[1] Dresselhaus MS, Chen G, Tang MY, Yang RG, Lee H, Wang DZ, et al. New directions for low-dimensional thermoelectric materials. Adv Mater 2007;19:1043–53.
[2] Zhang X, Zhao LD. Thermoelectric materials: energy conversion between heat and electricity. J Materiomics 2015;1:92–105.
[3] Yang J, Yip H-L, Jen AK-Y. Rational design of advanced thermoelectric materials. Adv Energy Mater 2013;3:549–65.
[4] Xiao C, Li Z, Li K, Huang PC, Xie Y. Decoupling interrelated parameters for designing high performance thermoelectric materials. Acc Chem Res 2014;47:1287–95.
[5] Jiang GY, He J, Fu CG, Zhu TJ, Liu XH, Hu LP, et al. High performance $Mg_2(Si,Sn)$ solid solutions: a point defect chemistry approach to enhancing thermoelectric properties. Adv Funct Mater 2014;24:3776–81.
[6] Li JF, Liu WS, Zhao LD, Zhou M. High-performance nanostructured thermoelectric materials. NPG Asia Mater 2010;2:152–8.
[7] Morelli DT, Jovovic V, Heremans JP. Intrinsically minimal thermal conductivity in cubic I-V-VI_2 semiconductors. Phys Rev Lett 2008;101.035901–1–4.
[8] Liu H, Shi X, Xu F, Zhang L, Zhang W, Chen L, et al. Copper ion liquid-like thermoelectrics. Nat Mater 2012;11:422–5.
[9] Qiu W, Xi L, Wei P, Ke X, Yang J, Zhang W. Part-crystalline part-liquid state and rattling-like thermal damping in materials with chemical-bond hierarchy. Proc Natl Acad Sci USA 2014;111:15031–5.
[10] Zhao LD, Lo SH, Zhang YS, Sun H, Tan GJ, Uher C, et al. Ultralow thermal conductivity and high thermoelectric figure of merit in SnSe crystals. Nature 2014;508:373–7.
[11] Heremans JP, Jovovic V, Toberer ES, Saramat A, Kurosaki K, Charoenphakdee A, et al. Enhancement of thermoelectric efficiency in PbTe by distortion of the electronic density of states. Science 2008;321:554–7.
[12] Heremans JP, Wiendlocha B, Chamoire AM. Resonant levels in bulk thermoelectric semiconductors. Energy Environ Sci 2012;5:5510–30.
[13] Pei YZ, Wang H, Snyder GJ. Band engineering of thermoelectric materials. Adv Mater 2012;24:6125–35.
[14] Li W, Chen ZW, Lin SQ, Chang YJ, Ge BH, Chen Y, et al. Band and scattering tuning for high performance thermoelectric $Sn_{1-x}Mn_xTe$ alloys. J Materiomics 2015;1:307–15.
[15] Pei YZ, Shi XY, LaLonde A, Wang H, Chen LD, Snyder GJ. Convergence of electronic bands for high performance bulk thermoelectrics. Nature 2011;473:66–9.
[16] Liu W, Tan XJ, Yin K, Liu HJ, Tang XF, Shi J, et al. Convergence of conduction bands as a means of enhancing thermoelectric performance of n-type $Mg_2Si_{1-x}Sn_x$ solid solutions. Phys Rev Lett 2012;108.166601–1–5.
[17] Tang YL, Gibbs ZM, Agapito LA, Li GD, Kim H-S, Nardelli MB, et al. Convergence of multi-valley bands as the electronic origin of high thermoelectric performance in $CoSb_3$ skutterudites. Nat Mater 2015;14:1223–8.
[18] Zide JMO, Vashaee D, Bian ZX, Zeng G, Bowers JE, Shakouri A, et al. Demonstration of electron filtering to increase the Seebeck coefficient in $In_{0.53}Ga_{0.47}As/In_{0.53}Ga_{0.28}Al_{0.19}As$ superlattices. Phys Rev B 2006;74.205335–1–5.
[19] Wang SY, Yang J, Wu LH, Wei P, Zhang WQ, Yang J. On intensifying carrier impurity scattering to enhance thermoelectric performance in Cr-doped $Ce_yCo_4Sb_{12}$. Adv Funct Mater 2015;25:6660–70.
[20] Liu HL, Yuan X, Lu P, Shi X, Xu FF, He Y, et al. Ultrahigh thermoelectric performance by electron and phonon critical scattering in $Cu_2Se_{1-x}I_x$. Adv Mater 2013;25:6607–12.
[21] Tritt TM, Subramanian MA. Thermoelectric materials, phenomena, and applications: a bird's eye view. MRS Bull 2006;31:188–98.
[22] Yang J, Zhang W, Bai SQ, Mei Z, Chen LD. Dual-frequency resonant phonon scattering in $Ba_xR_yCo_4Sb_{12}$ (R = La, Ce, and Sr). Appl Phys Lett 2007;90. 192111–1–3.
[23] Shi X, Yang J, Salvador JR, Chi MF, Cho JY, Wang H, et al. Multiple-filled skutterudites: high thermoelectric figure of merit through separately optimizing electrical and thermal transports. J Am Chem Soc 2011;133:7837–46.
[24] Puyet M, Lenoir B, Dauscher A, Pécheur P, Bellouard C, Tobola J, et al. Electronic, transport, and magnetic properties of $Ca_xCo_4Sb_{12}$ partially filled skutterudites. Phys Rev B 2006;73. 035126–1–12.
[25] Puyet M, Dauscher A, Lenoir B, Bellouard C, Stiewe C, Müller E, et al. Influence of Ni on the thermoelectric properties of the partially filled calcium skutterudites $Ca_yCo_{4-x}Ni_xSb_{12}$. Phys Rev B 2007;75.245110–1–10.
[26] Zhao WY, Wei P, Zhang QJ, Peng H, Zhu WT, Tang DG, et al. Multi-localization transport behaviour in bulk thermoelectric materials. Nat Comm 2015;6. 6197–1–7.

[27] Zhao WY, Wei P, Zhang QJ, Dong CL, Liu LS, Tang XF. Enhanced thermoelectric performance in barium and indium double-filled skutterudite bulk materials via orbital hybridization induced by indium filler. J Am Chem Soc 2009;131:3713–20.
[28] Zhao WY, Dong CL, Wei P, Guan W, Liu LS, Zhai PC, et al. Synthesis and high temperature transport properties of barium and indium double-filled skutterudites $Ba_xIn_yCo_4Sb_{12-z}$. J Appl Phys 2007;102. 113708–1–6.
[29] Ravel B, Newville M. Athena, Artemis, Hephaestus: data analysis for X-ray absorption spectroscopy using IFEFFIT. J Synchrotron Radiat 2005; 12:537–41.
[30] Payne MC, Teter MP, Allan DC, Arias TA, Joannopoulos JD. Iterative minimization techniques for ab initio total-energy calculations: molecular dynamics and conjugate gradients. Rev Mod Phys 1992;64: 1045–97.
[31] Mei ZG, Yang J, Pei YZ, Zhang W, Chen LD. Alkali-metal-filled CoSb3 skutterudites as thermoelectric materials: theoretical study. Phys Rev B 2008;77. 045202–1–8.
[32] Wee D, Kozinsky B, Marzari N, Fornari M. Effects of filling in $CoSb_3$: local structure, band gap, and phonons from first principles. Phys Rev B 2010;81. 045204–1–11.
[33] Christensen M, Iversen BB, Bertini L, Gatti C, Toprak M, Muhammed M, et al. Structural study of Fe doped and Ni substituted thermoelectric skutterudites by combined synchrotron and neutron powder diffraction and *ab initio* theory. J Appl Phys 2004;96:3148–57.
[34] Rehr JJ, Albers RC. Theoretical approaches to X-ray absorption fine structure. Rev Mod Phys 2000;72:621–54.
[35] Cao D, Bridges F, Chesler P, Bushart S, Bauer ED, Maple MB. Evidence for rattling behavior of the filler atom (*L*) in the filled skutterudites LT_4X_{12} (*L*=Ce, Eu, Yb; T=Fe, Ru; X=P, Sb) from EXAFS studies. Phys Rev B 2004;70. 094109–1–11.
[36] Baumbach R, Bridges F, Downward L, Cao D, Chesler P, Sales B. Off-center phonon scattering sites in $Eu_8Ga_{16}Ge_{30}$ and $Sr_8Ga_{16}Ge_{30}$. Phys Rev B 2005;71. 024202–1–19.
[37] Chakoumakos BC, Sales BC. Skutterudites: their structural response to filling. J Alloys Comp 2006;407:87–93.
[38] Grytsiv A, Rogl P, Michor H, Bauer E, Giester G. $In_yCo_4Sb_{12}$ skutterudite: phase equilibria and crystal structure. J Electron Mater 2013;42: 2940–52.
[39] Kitagawa H, Hasaka M, Morimura T, Nakashima H, Kondo S. Skutterudite structure and thermoelectric property in $Ce_fFe_{8-x}Co_xSb_{24}$ ($f = 0–2$, $x = 0–8$). Mater. Res Bull 2000;35:185–92.
[40] Singh DJ, Mazin II. Calculated thermoelectric properties of La-filled skutterudites. Phys Rev B 1997;56:R1650–3.
[41] Grosvenor P, Cavell RG, Mar A. X-ray photoelectron spectroscopy study of the skutterudites $LaFe_4Sb_{12}$, $CeFe_4Sb_{12}$, $CoSb_3$, and CoP_3. Phys Rev B 2006;74. 125102–1–10.
[42] Llunell M, Alemany P, Alvarez S, Zhukov VP, Vernes A. Electronic structure and bonding in skutterudite-type phosphides. Phys Rev B 1996; 53:10605–9.
[43] Chaput L, Pécheur P, Tobola J, Scherrer H. Transport in doped skutterudites: *Ab initio* electronic structure calculations. Phys Rev B 2005;72. 085126–1–11.
[44] Anno H, Matsubara K, Caillat T, Fleurial J-P. Valence-band structure of the skutterudite compounds $CoAs_3$, $CoSb_3$, and $RhSb_3$ studied by X-ray photoelectron spectroscopy. Phys Rev B 2000;62. 10737–1–7.
[45] Koga K, Akai K, Oshiro K, Matsuura M. Electronic structure and optical properties of binary skutterudite antimonides. Phys Rev B 2005;71. 155119–1–9.
[46] Lefebvre-Devos I, Lassalle M, Wallart X, Olivier-Fourcade J, Monconduit L, Jumas JC. Bonding in skutterudites: combined experimental and theoretical characterization of $CoSb_3$. Phys Rev B 2001;63. 125110–1–7.
[47] Thompson AC, Vaughan D. X-ray data booklet, Lawrence Berkeley laboratory. Berkeley: University of California; 1986.
[48] Hug G, Jaouen M, Barsoum MW. X-ray absorption spectroscopy, EELS, and full-potential augmented plane wave study of the electronic structure of Ti_2AlC, Ti_2AlN, Nb_2AlC, and $(Ti_{0.5}Nb_{0.5})_2AlC$. Phys Rev B 2005;71. 024105–1–12.
[49] Joseph B, Iadecola A, Simonelli L, Mizuguchi Y, Takano Y, Mizokawa T, et al. A study of the electronic structure of $FeSe_{1-x}Te_x$ chalcogenides by Fe and Se K-edge x-ray absorption near edge structure measurements. J Phys Condens Matter 2010;22. 485702–1–5.
[50] Ahmad S, Hoang K, Mahanti SD. *Ab Initio* study of deep defect states in narrow band-gap semiconductors: group III impurities in PbTe. Phys Rev Lett 2006;96. 056403–1–4.
[51] Hoang J, Mahanti SD. Electronic structure of Ga-, In-, and Tl-doped PbTe: a supercell study of the impurity bands. Phys Rev B 2008;78. 085111–1–8.
[52] Cutler M, Mott NF. Observation of Anderson localization in an electron gas. Phys Rev 1969;181:1336–40.
[53] Mahan GD, Sofo JO. The best thermoelectric. Proc Natl Acad Sci USA 1996;93:7436–9.

Dr. Ping Wei is currently working at the State Key Laboratory of Advanced Technology for Materials Synthesis and Processing, Wuhan University of Technology, China, as an associate professor. He received BS degree in materials science and engineering at Shandong University, China, in 2005, and was awarded MS degree and PhD in materials science both at Wuhan University of Technology in 2012. Then he worked at University of Washington as a research associate for three years, and came back to Wuhan University of Technology in 2015. His primary research focuses on the performance optimization and transmission electron microscopy studies of thermoelectric materials.

Professor Wenyu Zhao, Wuhan University of Technology Email: wyzhao@whut.edu.cn. Dr. Wenyu Zhao is a professor of State Key Laboratory of Advanced Technology for Materials Synthesis and Processing at Wuhan University of Technology (WUT) in China. He received Ph.D of materials science at WUT in 2004. He worked at WUT as an associate professor from 2003 to 2007 and then became a full professor in 2007. In 2009, he was supported by the program for New Century Excellent Talents in University awarded by the Ministry of Education of China. His research interests include thermoelectric materials, thermoelectric devices and power generation systems, and magnetic ferrite materials. He has authored and co-authored near 50 papers and 10 patents in these research areas.

Professor Qingjie Zhang, Wuhan University of Technology Email: zhangqj@whut.edu.cn. Prof. Qingjie Zhang received his Ph.D. from Huazhong University of Science and Technology in 1990. His research focuses on the thermoelectric materials and the related applications. At present, he is the Director of State Key Laboratory of Advanced Technology for Materials Synthesis and Processing at the Wuhan University of Technology (2005 to present) as well as the Chief Scientist of National 973 Program (2007–2017) in the field of thermoelectric materials.